The Utilization of Remotely Sensed Data to Analyze the Estimated Volume of Pyroclastic Deposits and Morphological Changes Caused by the 2010–2015 Eruption of Sinabung Volcano, North Sumatra, Indonesia

Fajar Yulianto,[1] Suwarsono,[1] and Parwati Sofan[1]

Abstract—In this research, remotely sensed data has been used to estimate the volume of pyroclastic deposits and analyze morphological changes that have resulted from the eruption of Sinabung volcano. Topographic information was obtained from these data and used for rapid mapping to assist in the emergency response. Topographic information and change analyses (pre- and syn- eruption) were conducted using digital elevation models (DEMs) for the period 2010–2015. Advanced spaceborne thermal emission and reflection radiometer (ASTER) global digital elevation model (GDEM) data from 2009 were used to generate the initial DEMs for the condition prior to the eruption of 2010. Satellite pour l'observation de la terre 6 (SPOT 6) stereo images acquired on 21 June 2015 and were used to make a DEM for that time. The results show that the estimated total volume of lava and pyroclastic deposits, produced during the period 2010 to mid-2015 is approximately 2.8×10^8 m³. This estimated volume of pyroclastic deposits can be used to predict the magnitude of future secondary lahar hazards, which are also related to the capacity of rivers in the area. Morphological changes are illustrated using cross-sectional analysis of the deposits, which are currently deposited to the east, southeast and south of the volcano. Such analyses can also help in forecasting the direction of the future flow hazards. The remote sensing and analysis methods used at Sinabung can also be applied at other volcanoes and to assess the threats of other types of hazards such as landslides and land subsidence.

Key words: Pyroclastic deposits, morphological change, remote sensing, SPOT 6, Sinabung volcano, North Sumatra, Indonesia.

1. Introduction

Among the developing countries, Indonesia is most vulnerable to natural hazards. This vulnerability is caused by the location of the nation at the confluence of three active tectonic plates, namely: Pacific, Euro-Asia, and Indo-Australia. The three plates slide past and collide with each other resulting in earthquakes, volcanic eruptions, landslides, floods and tsunami. Natural hazards resulting from these events are the consequence of the combination of the natural events and human processes (Sutikno 2007; Yulianto 2014; Yulianto et al. 2013, 2015a).

An important control on the occurrence of natural hazards is topography (Darmawan 2012; Charbonnier et al. 2013; Yulianto et al. 2015b). Topography has a dominant influence on the potential and direction of a hazard, such as volcanic eruptions, landslides, and floods (Felpeto et al. 2007; Yulianto 2014). Thus, the availability of topographic data and up-to-date information (including post-hazards topography) is needed to predict and prevent potential hazards in the future and minimize the risk of natural hazards.

Up-to-date topographic information can be obtained by direct measurement in the field and indirectly using remote sensing data. Direct measurement can be done with the terrestrial surveying techniques such as electronic distance measurement (EDM), global positioning system (GPS), tilt and leveling. Indirect measurements can be performed with the use of remote sensing data and combined with available of spatial data, such as topographic maps (Stevens et al. 1999; Kriswati et al. 2012; Yulianto et al. 2015b). Both types of techniques have strengths and weaknesses. Direct measurements in the field can provide results with excellent accuracy and high resolution, but such techniques are time intensive, expensive and too dangerous, given the current activity. Indirect measurement with remote sensing data can shorten the time of acquisition, but

[1] Remote Sensing Application Center, Indonesian National Institute of Aeronautics and Space (LAPAN), Jl. Kalisari No. 8, Pekayon, Pasar Rebo, Jakarta 13710, Indonesia. E-mail: fajar.lapan.rs@gmail.com; fajar.yulianto@lapan.go.id

have limitations with respect to resolution and accuracy of the results (Murray 1990; Stevens et al. 1999; Hayakawa et al. 2008; Tachikawa et al. 2011; Hashimoto 2013; Becek 2014; Prush and Lohman 2015; Tadono et al. 2015).

Rapid mapping during emergency responses is acutely needed to implement disaster mitigation practices. Remotely sensed data have been effectively used to support the needs of emergency response (e.g., Brivio et al. 2002; Surono et al. 2012; Pallister et al. 2013; Yulianto et al. 2015a). Topographic information to support these activities can be simplified by using digital elevation models (DEMs) as demonstrated by the work of Hirano et al. (2003), Huggel et al. (2008), Mukherjee et al. (2013), Czubski et al. (2013) and others. The use of remotely sensed topography in disaster mitigation has increased dramatically in the past decade. Examples include use of ASTER and shuttle radar topography mission (SRTM) digital elevation models (DEMs), as well as data from SPOT, advanced land observing satellite (ALOS) panchromatic remote-sensing instrument for stereo mapping (PRISM) and phased array type L-band synthetic aperture radar (PALSAR), environmental satellite (ENVISAT), radio detection and ranging satellite (RADARSAT), cartography and satellite (CARTOSAT), and constellation of small satellites for the Mediterranean basin observation (COSMO)-SkyMed, among others (e.g., Buyuksalih et al. 2005; Kornus et al. 2006; Trisakti and Julzarika 2011; d'Ozouville et al. 2008; Toutin 2010; Sambodo and Soleh 2011; Yulianto 2014; Yulianto et al. 2015b, Giribabu et al. 2013; Bignami et al. 2013). In addition to these spaceborne systems, airborne remote sensing has been effectively used to produce high-resolution topographic data for disaster management (e.g., Bater and Coops 2009; Diefenbach et al. 2012). Results from these studies have enabled detection and interpretation of stages and processes more quickly and efficiently than would have been possible using with direct measurements in the field.

In monitoring volcano eruptions, one of the benefits of topographic data is to estimate the volume of erupted material deposited and analyze morphological changes. Such changes can be used to forecast the impact of volcanic activity in the future (e.g.,

Pallister et al. 1992, 2013; Stevens et al. 1999; Surono et al. 2012; Charbonnier et al. 2013; Bignami et al. 2013).

Stevens et al. (1999) conducted a classic study of morphologic changes at Mount Etna Sicily. We use this study as a model for our work at Sinabung volcano. In the Stevens et al. (1999) study, pre-eruption and post eruption topographic maps of Mount Etna were used to create DEMs. Contours on the topographic maps were digitized and the resulting point data were interpolated to produce triangular irregular networks (TINs), which in turn were used to generate pre- and post-eruption DEMs. These DEMs were then used to estimate the volume of lava flows and changes in morphology resulting from the 1981 and 1983 eruptions at Mount Etna. Using a similar method of comparing pre- and post-eruption surfaces, Yulianto (2014), Yulianto et al. (2015b) analyzed morphological change as a result of the 2010 eruption of Merapi volcano, Central Java, Indonesia. In this case, ALOS PALSAR data were used to produce DEMs and to detect subtle pre-and post-eruption surface changes by the interferometry synthetic aperture radar (InSAR) method. Cross-sections were then constructed to describe the morphological changes in the study area.

Limited availability of topographic data during the recent eruptions of Sinabung volcano has been an obstacle in analyzing morphologic change and in obtaining volumes of pyroclastic materials. To address this problem, we extracted a 2015 DEM from SPOT 6 stereo images, which have a spatial resolution of 6 m. By comparing our new DEM with pre-eruption topographic maps we are able to estimate the volume of pyroclastic flow deposits and morphological changes for the period 2010–2015.

2. Study Area and Summary of Recent Eruptions

Our study area is Sinabung volcano (3°10′12″N and 98°23′31″E, 2460 m elevation), is located in North Sumatra, Indonesia. The volcano is a predominantly andesitic–dacitic stratovolcano formed during Plestocene to Holocene with an elevation of 2460 m (Chaussard and Amelung 2012; González et al. 2014). It is administratively in the Karo

Highlands, Karo District, North Sumatra, Indonesia (Fig. 1), which had a 2013 population of 363,755 and a population density is 171 inhabitants/km^2 (Indonesian Central Agency of Statistic 2013).

Before 2010, the volcano was classified as a type B stratovolcano by Indonesia's Center for Volcanology and Geologic Hazard Mitigation (CVGHM), because it had not erupted since the 1600s. The
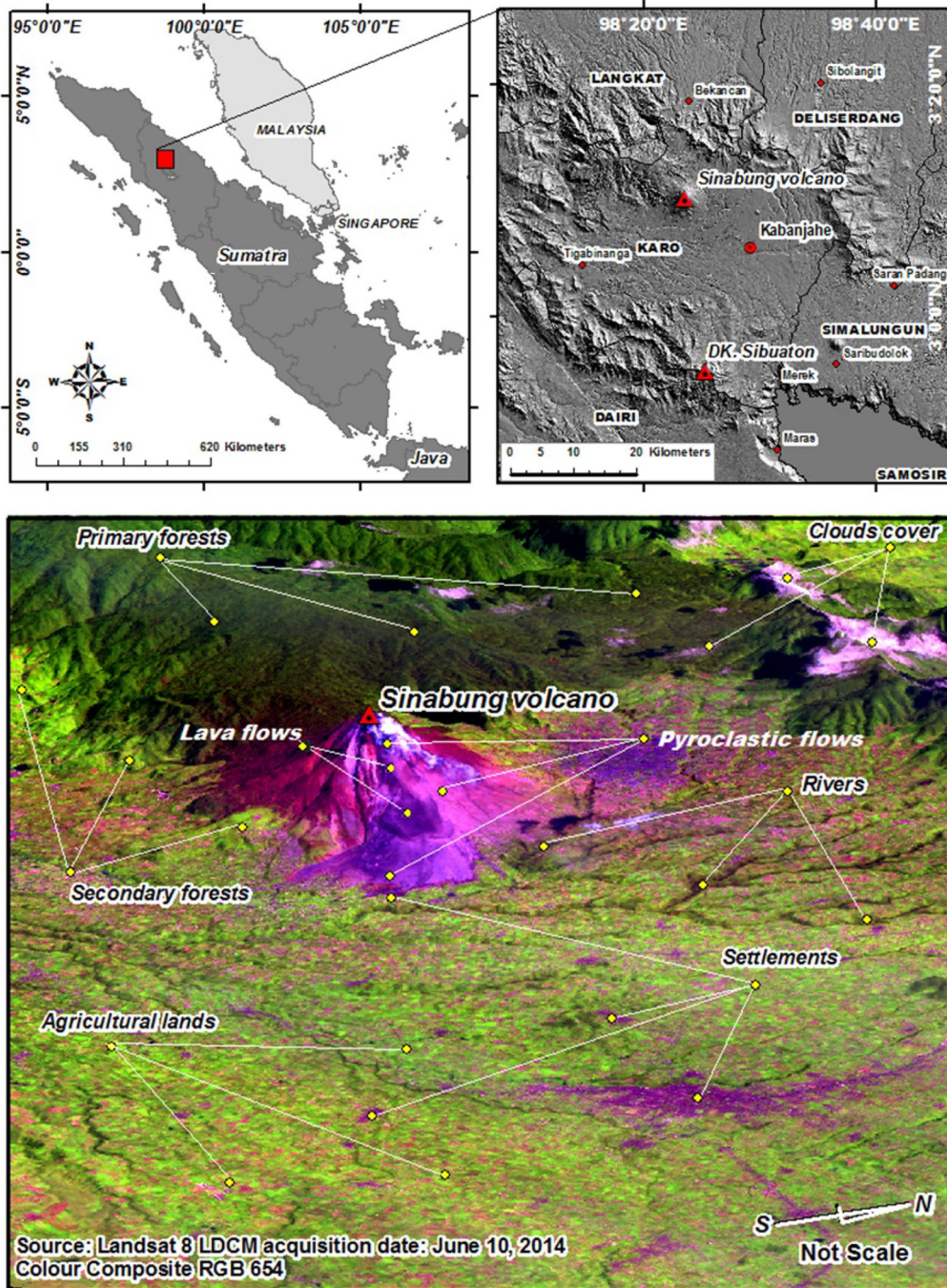

Figure 1
Research area at Sinabung volcano in North Sumatra, Indonesia Source: Landsat 8 LDCM data was acquired by LAPAN, 2014

Table 1

Sinabung volcano eruption history of the period 2010–2015 Source: Summarized from CVGHM (2015)

Period of time	Run out distance (in meter)	Height of volcanic ash column (in meter)	Material eruption	Status of volcanic activity
27 August 2010	–	–	Vas	–
28 August–07 September 2010	–	500–5000	Vas; SGm	Level IV (*Awas*)
15 September 2013	–	–	Vas; SGm	Level II to III (*Waspada* to *Siaga*)
17 September 2013	–	3000	Vas; SGm	–
18 September 2013	–	1500	Vas; SGm	–
15 October–03 November 2013	–	600–700	Vas	Level II to III (*Waspada* to *Siaga*)
04–24 November 2013	100–1000	500–10,000	Vas; SGm; Pfw	
29 November 2013	–	–	Vas	Level III to IV (*Siaga* to *Awas*)
04–30 December 2013	500	800–2000	Vas; SGm; Pfw	–
01–31 January 2014	500–4500	500–5000	Vas; SGm; Pfw	–
01–29 February 2014	1000–4500	500–2000	Vas; SGm; Pfw	–
01–31 March 2014	1000–2000	–	Vas; Pfw	–
01–30 April 2014	500–2500	–	Vas; Pfw	–
01–31 May 2014	500–3000	–	Vas; Pfw	–
01–30 June 2014	–	4000	Vas	–
01–31 July 2014	2000–4000	–	Pfw	–
01–31 August 2014	500–1500	–	Pfw	–
01–31 September 2014	500–3000	2000	Vas; SGm; Pfw	–
01–31 October 2014	500–3000	–	Vas; Pfw	–
01–30 November 2014	1000–4000	–	Vas; Pfw	–
01–31 December 2014	1000–4500	–	Vas; Pfw	–
01–31 January 2015	500–3500	–	Vas; Pfw	–
01–28 February 2015	1000–4500	–	Vas; Pfw	–
01–31 March 2015	2000–4700	–	Vas; Pfw	–
01–30 April 2015	1000–4900	–	Vas; SGm; Pfw	–
22 June and 25–29 June 2015	4500	–	Vas; Pfw	–

Explanation: *Vas* volcanic ash, *SGm* sand-gravel material, *Pfw* pyroclastic flows

volcano was re-classified as type A in 2010, due to short-lived phreatic eruptions that began on 27 August, 2010. The volcano was then quiet until September 2013 when new eruptions began. It has remained in eruption, producing lava and block-and-ash (Merapi type) pyroclastic flows since that time until now (2015) (Chaussard and Amelung 2012; González et al. 2014).

The eruptions of 2010–2015 have included phreatic and magmatic phases as summarized in Table 1. The magmatic eruptions produced lava domes and lava flows, both of which collapsed to produce block-and-ash type pyroclastic flows. Ash columns associated with the collapses have ranged from a few hundred meters to about 5 km above the volcano's summit.

The first eruption in 2013 took place on 15 September and produced a volcanic ash column and a burst of incandescent rock around the crater.

Consequently, CVGHM raised the alert status from Level II (*Waspada*) to Level III (*Siaga*). On 17–18 September, ash columns reached 1500–3000. Following a period of reduced activity on 29 September, 2013 the volcano activity status was downgraded from Level III (*Siaga*) to Level II (*Waspada*). However, on 15 October to 3 November, 2013 eruptions again produced volcanic ash columns of 600–5000 m and a new fracture on the north flank of Sinabung volcano formed with a length of approximately 500 m. On 3 and 4 of November 2013 the activity was again increased to Level III (*Siaga*), and volcanic ash columns associated with lava-dome collapse reached altitudes of 500–10,000 m. Pyroclastic flows associated with these dome-collapse eruptions spread southeast to east, and reached distances of 100 to about 1000 m. On 24 November to 30 December 2013 the status of Sinabung volcano was increased from Level III (*Siaga*) to Level IV (*Awas*). Ash

column heights ranged from 500 to 5000 m and pyroclastic flows spread to the southwest and west as well as in the east to southeast sectors, where they reached distances of 500 to 4000 m from the summit. On 1 February 2014, 15 people were killed in the village Sukameriah, when the flank of a lava flow collapsed and produced a pyroclastic flow, and a surge that swept through the village. Eruptions during 1–29 February 2014 produced column heights of 500–2000 m pyroclastic flows and surges that reached 1000–4000 m to the south-southeast. In addition, 2015 eruptions destroyed about 50 houses in the village Gurukinayah and eruptions on 2–28 April 2015 resulted in pyroclastic flows and surges that reached distances of 1000–4000 m and ash columns to heights of 3500 m (CVGHM 2015).

3. Methodology

3.1. Data Availability

For our research we derived a pre-eruption DEM from ASTER GDEM version 1.0 (released 29 June 2009) and SPOT 6 stereo image data, which was acquired on 21 June 2015 (Fig. 2). In addition, the SRTM DEM data in year 2000 (released to the public on 23 September 2014 was used as input data to obtaining ground control points (GCP's). These data were then used for creating and extracting the DEM from SPOT 6 stereo images. Additionally, topographic maps with a scale of 1:50,000 from the Indonesian geospatial information agency (BIG) were used as reference data to evaluate accuracy of the SPOT 6 DEM.

3.2. Data Processing and Analysis

3.2.1 Digital Elevation Model (DEM) Extraction

The pre-eruption DEM data is from ASTER GDEM version 1.0 with a spatial resolution of 30 m. It was necessary to resize the ASTER GDEM data to obtain similarity with the syn-eruption DEM with its spatial resolution of 6 m. To do so, we extracted values of raster points from the ASTER GDEM to get an elevation point distribution, and combined this with a data distribution derived from on the topographic map scale of 1:50,000. The results of merging the elevation data point distributions of ASTER GDEM and topographic maps was done by interpolating points at a pixel size of 6 m using an inverse distance weighted (IDW) approach, using the methods of Su and Bork (2006) and Bater and Coops (2009).

Our syn-eruption DEM was obtained by extraction from the SPOT 6 stereo images using ENVI 5.0 software with the Exelis visual information solution. There are three stages to make a DEM data extraction from SPOT 6 stereo images, namely: epipolar image creation, image matching, and DEM geocoding. Epipolar geometry describes geometrical constraints between two stereo images, and ensures that both the image frames have a ground point and centers that lie in the same plane. In the second stage, image matching is performed to find conjugate points on the two image frames. The output of this stage is called a parallax image, in which epiporal lines between the left and right image are stored and is used to build the DEM. In the third stage, DEM geocoding is used to re-project the DEM to the output map projection. In this research, the study area has a WGS 1984 datum projection with the universal transverse mercator (UTM) zone 47 north. The reference data that is used to provide GCPs is the SRTM DEM. Furthermore, the absolute orientation of the computed terrain models can be run at this stage. Details of the process may be found at (http://www.exelisvis.com/).

Accuracy was calculated to determine the error of the DEM data generated from the extraction of SPOT 6 stereo images. In this calculation, the values of the elevation points of the topographic map (1:50,000-scale) were used as a reference. The calculation is expressed in root mean square error, which can be presented in Eq. 1 (e.g., Marfai and King 2007; Yulianto et al. 2015b).

$$\text{RMSE} = \sqrt{\frac{1}{n}\sum_{i=1}^{n}(\text{Zdem\_ref} - \text{Zdem\_mod})^2} \quad (1)$$

where RMSE is the value of root mean square error. Zdem_ref is the value of elevation in the DEM reference. Zdem_mod is the value of elevation in the

Figure 2
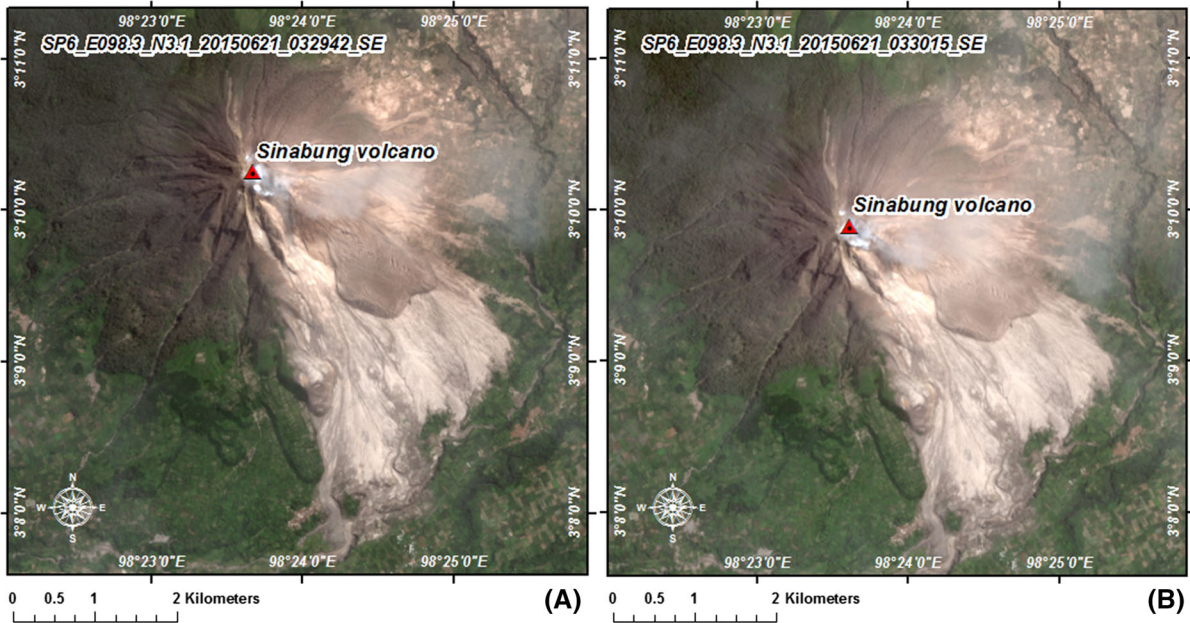
SPOT 6 stereoimages at Sinabung volcano. **a** Dataset ID:SEN_SPOT6_ 20150621_032942900_000, *acquisition date* June 21, 2015, *time* 03:29:42.7, *orientation angle* +356.62°, *incidence angle* +18.45°, *sun azimuth* +52.42°, *sun elevation* +54.97° and **b** dataset ID: SEN_SPOT6_20150621_033015100_000, *acquisition date* June 21, 2015, *time* 03:30:15.0, *orientation angle* +263.96°, *incidence angle* +5.37°, *sun azimuth* +52.29°, *sun elevation* +55.08°.) Source: Lapan, 2015

DEM model. n is the number of point elevations used for calculation of the RMSE value.

3.2.2 The Estimated Volume of Pyroclastic Deposited

As there has been on limited syn-eruption erosion, the approximate volume estimated of pyroclastic flows deposits from eruption of Sinabung volcano during the period 2010 to mid-2015 can be calculated by differencing the pre- and syn-eruption DEM data for this period. Thickness of pyroclastic flows is assumed to be equal to the difference values of elevation in the DEM pre- and syn-eruption data, which is formulated in Eq. 2 (see also for comparison, Daag and Van Westen 1996).

$$\Delta LTF = DEMt2 - DEMt1 \qquad (2)$$

where ΔLTF is pyroclastic flow thickness or the difference in elevation between the data pre- and syn-eruption. DEMt2 is the DEM syn-eruption (DEM data from the extraction using SPOT 6 stereo images). DEMt1 is the DEM pre-eruption (DEM data

was derived based on the IDW interpolation from ASTER GDEM in 2009 and merged with the elevation points from the topographic map.

The volume of pyroclastic flow deposits can be formulated as shown in Eq. 3 (see Stevens et al. 1999, for comparison).

$$VolLF = \sum_{l,l}^{m,n} xy \Delta LTF_{i,j} \qquad (3)$$

where VolLF is the volume pyroclastic flow deposited. x and y are the pixel dimensions. m and n are the array of elevation change columns and rows. ΔLTF is the pyroclastic flows thickness for each pixel position (i, j).

In this research, uncertainty propagation for volumes can be calculated by the standard deviation of the volume for most pessimistic value and for more optimistic value, which is formulated in Eqs. 4–6. Based on research conducted by Wang et al. (2011), ASTER GDEM is known to have its own uncertainties, and a global comparison between SRTM DEM model and ASTER GDEM model showed a

systematic difference of ~ 5.6 m, with a standard deviation of 5 m. Due to the limitations and lack of ground true and GPS Ground Control Points, then a reasonable assumption is to add and propagate the 5 m uncertainties.

$$\mathrm{Vol}_{\mathrm{std}_1} = n * A * \mathrm{Sigma} \qquad (4)$$

$$\mathrm{Vol}_{\mathrm{std}_2} = A * \sqrt{n * \mathrm{Sigma}} \qquad (5)$$

$$\mathrm{Sigma} = \sqrt{(\mathrm{sig\_ASTER})^2 + (\mathrm{sig\_SPOT6})^2} \qquad (6)$$

where $\mathrm{Vol}_{\mathrm{std}_1}$ is the standard deviation of volume for most pessimistic value. $\mathrm{Vol}_{\mathrm{std}_2}$ is the standard deviation of volume for more optimistic value. n is the number of pixels. A is the area of the pixel in m^2. Sigma is the uncertainty in m, (sig_ASTER is the uncertainty for ASTER GDEM data, and sig_SPOT6 is the is the uncertainty for SPOT 6 DEM data).

3.2.3 Morphological Change Detection Analysis

In this research, morphological change detection analysis can be done by comparing the locations expected to experience change in elevation on the condition pre- and syn- eruption. The analysis is done by creating a cross-section model at several location changes based on the DEM data pre- and syn-eruption. Cross-section or profile models can be used to describe the occurrence of morphological changes (e.g., Yulianto 2014; Yulianto et al. 2015b; Solikhin et al. 2015). Our profiles were constructed perpendicular to the direction of the eruption deposits that occurred during the period 2010–2015. Thus, variations in the morphological changes can be seen clearly in the profiles.

4. Results

Results of the process of merging and interpolation to resolve a pixel size of 6 m are presented in Fig. 3a, c. Meanwhile, the results of DEM syn-eruption from processing and extraction SPOT 6 stereo images are presented in Fig. 3b, d. Vertical accuracy is only calculated for the results of the DEM data that are extracted from the SPOT 6 stereo images. The DEM data of 2009 are used as a baseline and are assumed to be correct. A total of 2495 points from

the 1:50,000 scale topographic map are used as a basic reference in determining the value of RMSE. Elevation points that did not change as a consequence of the eruption were selected for this calculation and yielded a RMSE of 9.36 m. Standardized residuals for the RMSE calculation are presented in Fig. 4.

Thicknesses of pyroclastic deposits were calculated based on the difference in height of the DEM data pre- and syn-eruption. The results of the thickness information can be divided into several classes at intervals of each layer thickness in the range of 25 m. A layer with a thickness of <25 m has the most extensive area zoning with a measured total area of 1,773,216 m^2. In contrast, the layer with the smallest area is in the range of 201–225 m, and a measured total area of 23,148 m^2. Spatially, the resulting distribution of pyroclastic material deposits in the research area is presented in Fig. 5. Figure 5a shows the visual appearance of pyroclastic deposits from a Landsat 8 image acquired on 29 June 2015. Figure 5b shows our calculated thicknesses of pyroclastic deposits, based on the elevation differences between the pre- and syn-eruption DEM data.

The thickness data shown in Fig. 5b are used to calculate the estimated volume of the pyroclastic deposits from the eruption by multiplying pixel image area times the thickness intervals fort these pixels. The calculations were performed for intervals of 25 m in thickness and the results for each of these ranges and a total volume for the eruption ($\sim 2.8 \times 10^8$ m^3) are given in Table 2.

Table 3 quantifies the extent of morphological change during the eruption period of 2010–2015 as the maximum change (positive or negative) in elevation along the profile lines located in Fig. 6 and shown as Figs. 7, 8, 9, 10, and 11. Changes resulting from areas subjected to either pyroclastic sedimentation or lava flow deposition are process $(+)$, whereas erosion is negative $(-)$.

5. Discussion

The methods applied here can be done rapidly once clear satellite data are available, and, therefore, they are useful to quickly estimate morphologic change, including areas and volumes of new deposits
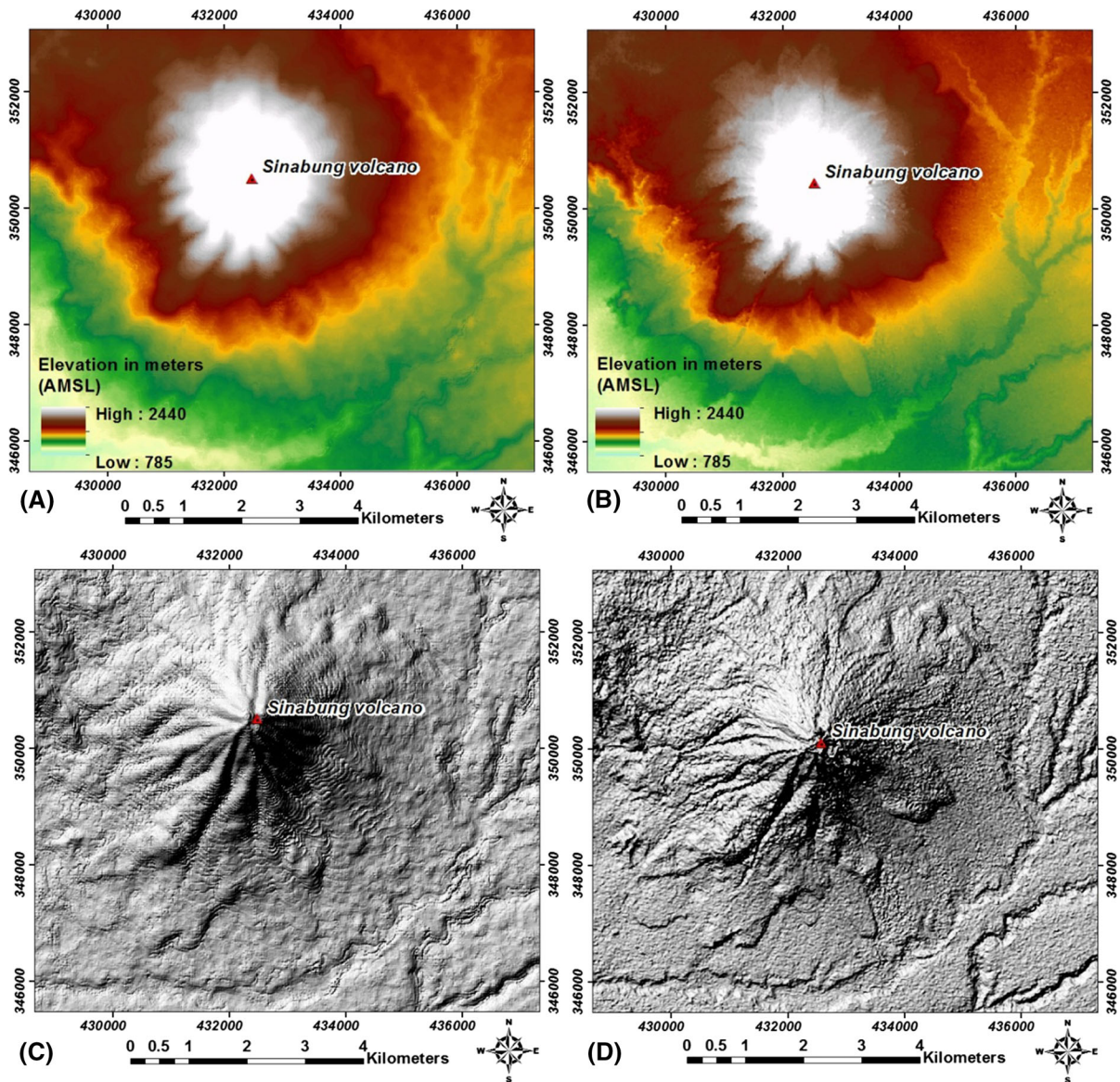
Figure 3
Comparison of the DEM data with the acquisition of Sinabung volcano during period 2010–2015. **a** Image showing the 2010 DEM data, processed and merged with ASTER GDEM data and with 1:50,000-scale topographic map data and interpolated to a pixel size of 6 m using an inverse distance weighted technique. **b** Image showing results of processed and extracted DEM from 2015 SPOT 6 stereo images, with a spatial resolution is 6 m. **c** Hillshade image of the DEM data. **d** Hillshade image of the 2015 DEM image of Sinabung volcano

during an ongoing eruption crisis. As we calculate only DEMs, as opposed to bare-earth digital terrain models (DTM) the elevation changes we calculate include canopy and man-made structures. However, these errors are small in our study, because the pre-eruption canopy height in the pyroclastic fan area was generally <10 m and for the syn-eruption images there are no trees.

The calculation of total volume of pyroclastic material and lava erupted in the period 2010 to mid-2015 is $\sim 2.8 \times 10^8$ m^3, with uncertainties of the standard deviation of volume for most pessimistic
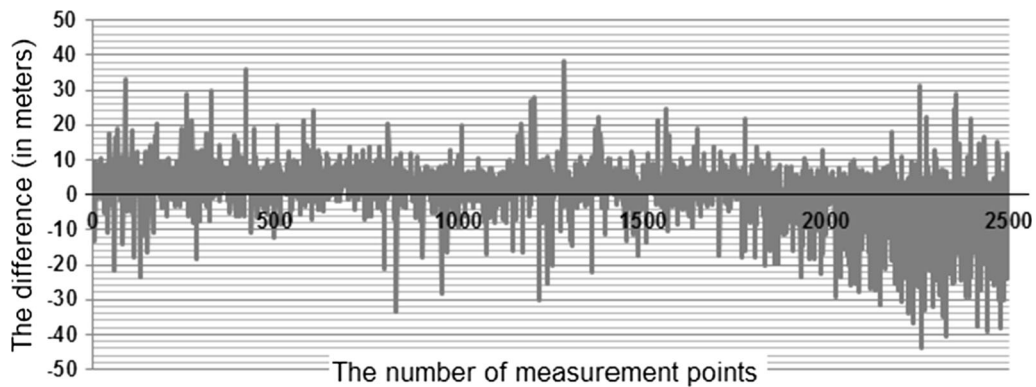
Figure 4
Standardized residuals error plot for RMSE calculation of of the DEM SPOT 6 and topographic map
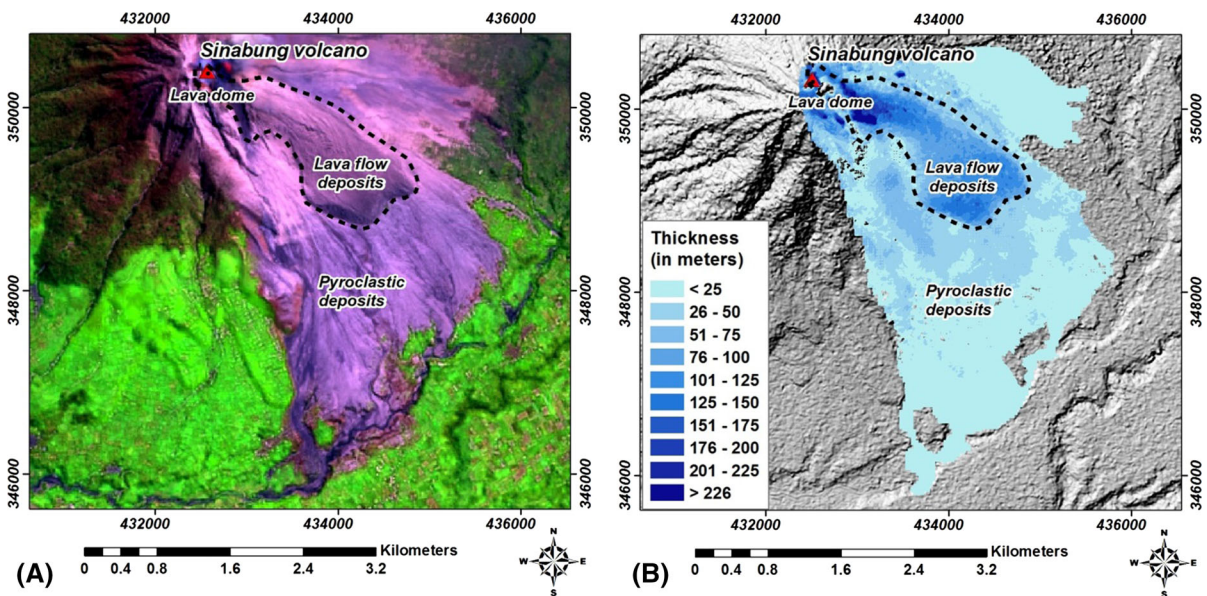

Figure 5
Spatial distribution of pyrocalastic and lava deposits in the research area. **a** The visual appearance of the deposits from Landsat 8 LDCM was acquired by LAPAN, 2015. **b** Thickness of pyroclastic and lava flow deposits based on the difference in elevation between the value of the pre- and syn- eruption data (in meters)

value is $\sim 0.6 \times 10^8$ m^3 and for more optimistic value is $\sim 0.5 \times 10^5$ m^3. We have calculated the volume of lava separately from the volume of pyroclastic deposits, comprising $\sim 0.9 \times 10^8$ m^3 of lava flow and dome deposits, and $\sim 1.9 \times 10^8$ m^3 of pyroclastic deposits. The calculation is performed separately, because the lava flow deposits and pyroclastic deposits have different characteristics. The lava flow deposits, a material eruption that is not easily eroded, while the pyroclastic deposits, a material eruption that is easily eroded and separated.

The volume of pyroclastic deposits produced during the period of the eruption can be used as input to forecast the secondary impacts of lahar hazards eruption in the area. For example, we can evaluate the capacity of the riversin the area to determine whether they can accommodate the total potential volume of sediment and lahar deposits that may be produced in

Table 2

The results of the calculation of the estimated volume of pyroclastic flows deposits caused by the 2010–2015 eruption of Sinabung volcano

Class of thickness (m)	Number of pixels	Areas (m^2)	Approximate estimation volume (in $\times 10^8$ m^3)	Uncertainties vol_std$_1$ for most pessimistic value (in $\times 10^8$ m^3)	Uncertainties vol_std$_2$ for more optimistic value (in $\times 10^5$ m^3)
<25	49,256	1,773,216	0.252	0.188	0.260
26–50	46,491	1,673,676	0.615	0.178	0.253
51–75	19,433	699,588	0.428	0.074	0.163
76–100	14,075	506,700	0.447	0.054	0.139
101–125	12,183	438,588	0.491	0.047	0.129
126–150	4700	169,200	0.230	0.000	0.008
151–175	1838	66,168	0.107	0.007	0.050
176–200	1209	43,524	0.082	0.005	0.041
201–225	643	23,148	0.049	0.002	0.030
>226	1091	39,276	0.096	0.004	0.039
Total	150,919	5,433,084	2.797	0.576	0.456

Table 3

Analysis of morphological changes of the DEM pre- and syn- eruption in the period 2010 to mid-2015 in the research area

Spatial profile	Change of the DEM pre- and syn- eruption (in meters)			
	1	2	3	4
A-A'a	180 (+)	110 (−)	150 (−)	0
A-A'b	0	200 (+)	50 (+)	30 (+)
A-A'c	0	75 (+)	130 (+)	25 (+)
A-A'd	35 (+)	125 (+)	130 (+)	30 (+)
A-A'e	30 (+)	25 (+)	100 (+)	25 (+)

" +" sedimentation, "−" indication of the collapsed volcanic deposits with limited syn-eruption erosion, and "0" no change

the future. If the capacity of the river cannot accommodate this amount of material then these future lahars and floods will likely overflow the river channels and damage the environment (including residential communities) nearby. This information can be used in relocation planning of residential areas or other objects, with the aim to minimize the secondary effect of the eruption. The morphological changes in the research area have predominated in the east-southeast to south sectors. Analysis related to morphological changes of the volcano can also be used to forecast the direction of lava flows and pyroclastic flows in the future.

6. Conclusion

The purpose of this research is to describe the use of remotely sensed data to estimate the volume of pyroclastic material deposited and to analyze morphological change as a result of the eruption of Sinabung volcano during the period 2010–2015. A limitation on the availability of high resolution topographic data for the area affected by the eruption has been a problem in determining such volumes. Thus, data from SPOT 6 stereo images in 2015 have been used to create a DEM for the research area. This DEM has a vertical error based on reference points in areas that have not changed of less than 10 m, enabling a first approximate estimation of 2.8×10^8 m^3 for the total volume of eruptive products, comprising $\sim 0.9 \times 10^8$ m^3 of lava flow and dome deposits, and $\sim 1.9 \times 10^8$ m^3 of pyroclastic deposits. As relatively little erosion of the deposits had taken place by the time of the SPOT images (21 June 2015), we take these volumes to be representative of the total eruption volume at this time. The availability of other image data that has a higher resolution, such as light detection and ranging (LiDAR), TerraSAR-X and detailed field surveys
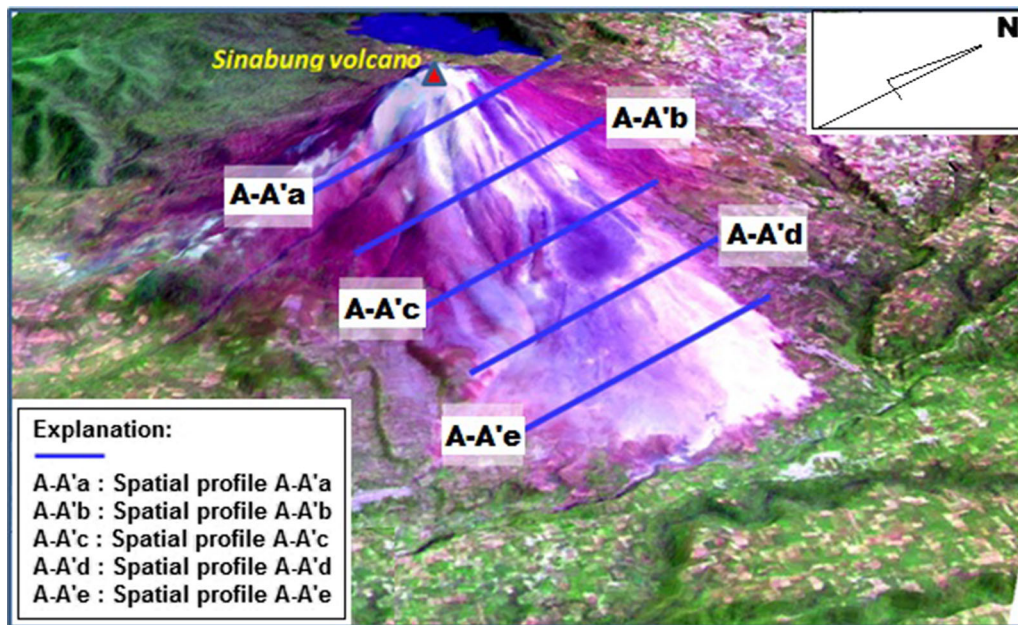
Figure 6
Oblique projection of Sinabung volcano showing locations of profiles in Figs. 7, 8, 9, 10 and 11. As an oblique projection, this image has a variable scale. Diameter of the volcano is approximately 7–8 km
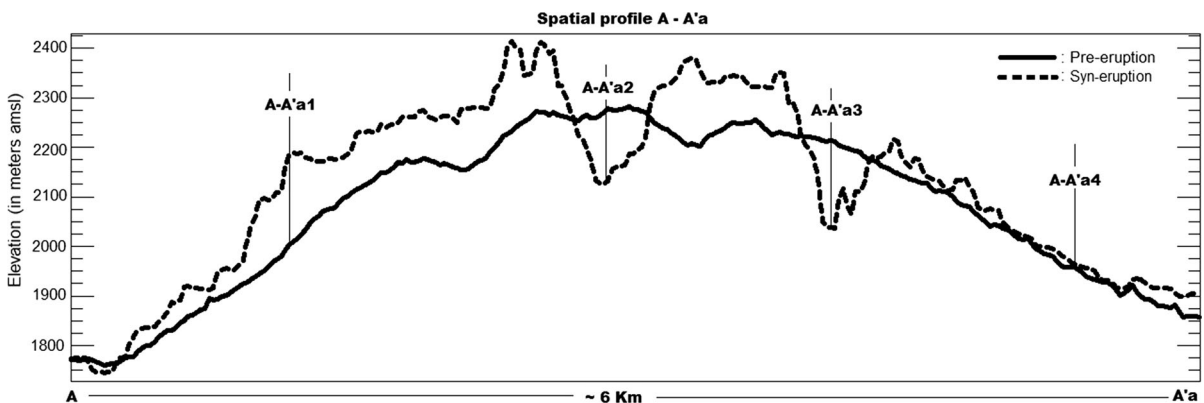

Figure 7
Spatial profile A-A′a

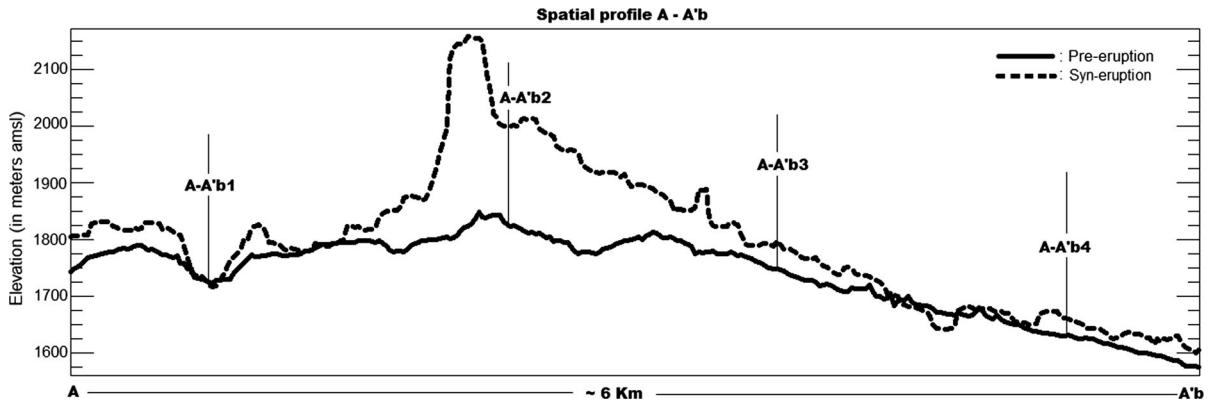these data can later be used to compare and improve our results.

Figure 8
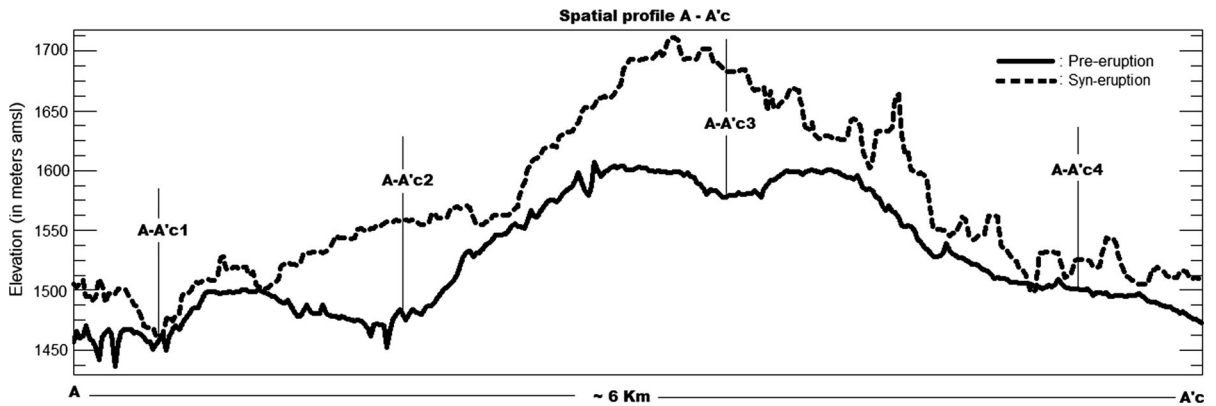Spatial profile A-A′b
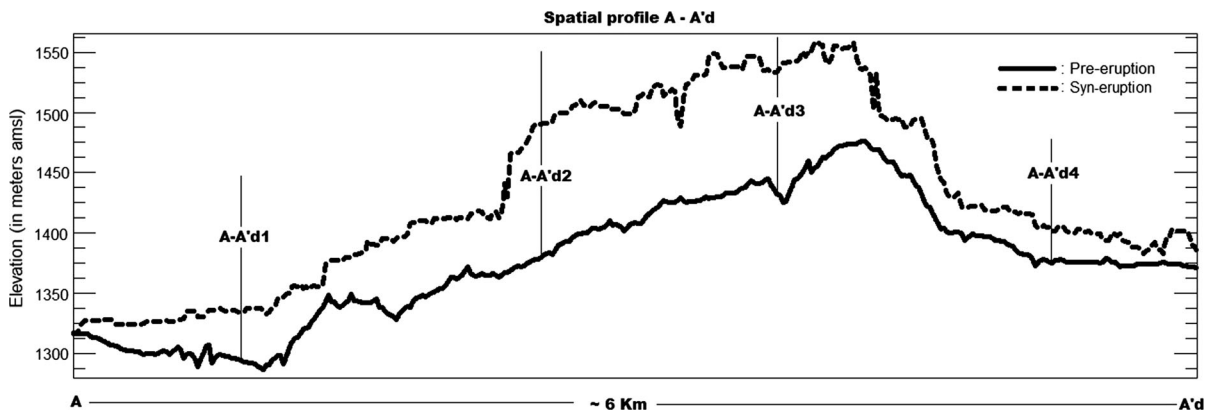

Figure 9
Spatial profile A-A′c
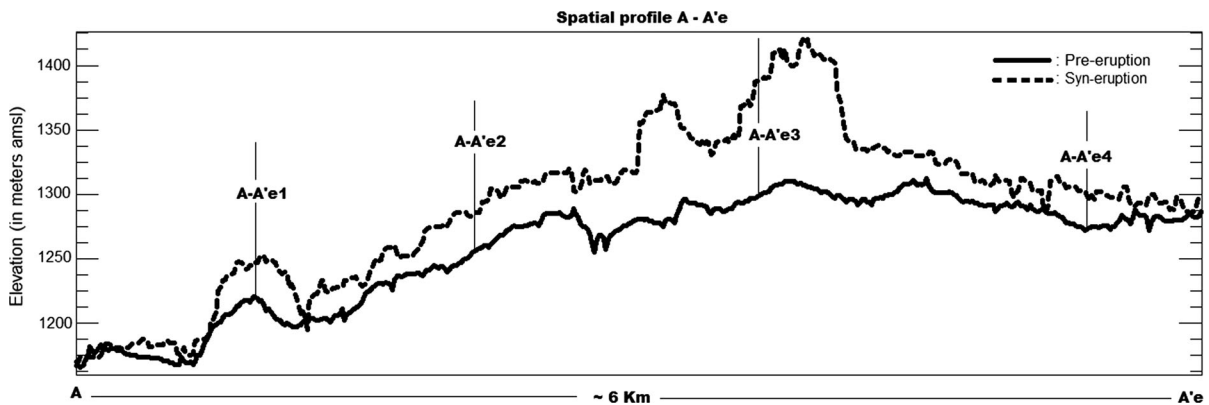

Figure 10
Spatial profile A-A′d

Figure 11
Spatial profile A-A′e

Maulana, MBA., Dr. Wikanti Asriningrum and our colleagues at the Remote Sensing Application Center, LAPAN for discussions and suggestions, and two anonymous reviewers were very helpful in improving our manuscript. SPOT 6 stereo images data and Landsat 8 LDCM data were provided by Remote Sensing Technology and Data Center, LAPAN. ASTER GDEM data were provided by the Japan-US ASTER Science Team. Topographic maps were provided by the Indonesian Geospatial Information Agency (BIG).

REFERENCES

Bater, C. W., & Coops, N. C. (2009). Evaluating error associated with LiDAR-derived DEM interpolation. *Computers & Geosciences, 35*(2), 289–300.

Becek, K. (2014). Assessing global digital elevation models using the runway method: the advanced spaceborne thermal emission and reflection radiometer versus the shuttle radar topography mission case. *Geoscience and Remote Sensing, IEEE, 52*(8), 4823–4831.

Bignami, C., Ruch, J., Chini, M., Neri, M., & Buongiorno, F. (2013). Pyroclastic density current volume estimation after the 2010 Merapi volcano eruption using X-band SAR. *Journal of Volcanology and Geothermal Research,*. doi:10.1016/j.jvolgeores.

Brivio, P. A., Colombo, R., Maggi, M., & Tomasoni, R. (2002). Integration of remote sensing data and GIS for accurate mapping of flood areas. *International Journal of Remote Sensing, 23*(3), 429–441. doi:10.1080/01431160010014729.

Buyuksalih, G., Kocak, G., Topan, H., Oruc, M., & Marangoz, A. (2005). SPOT revisited: accuracy assessment, DEM generation and validation from stereo SPOT 5 HRG images. *The Photogrammetric Record, 20*(110), 130–146.

Charbonnier, S. J., Germa, A., Connor, C. B., Gertisser, R., Preece, K., Komorowski, J. C., et al. (2013). Evaluation of the impact of the 2010 pyroclastic density currents at Merapi volcano from high-resolution satellite imagery, field investigation and numerical simulations. *Journal of Volcanology and Geothermal Research, 261*, 295–315.

Chaussard, E., & Amelung, F. (2012). Precursory inflation of shallow magma reservoirs at west Sunda volcanoes detected by InSAR. *Geophysical Research Letters, 39*, L21311. doi:10.1029/2012gl053817.

CVGHM (2015). Evaluation of Sinabung volcano observation until June 2nd, 2015. http://www.vsi.esdm.go.id/ Cited June 05, 2015 (In Indonesian).

Czubski, K., Kozak, J., & Kolecka, N. (2013). Accuracy of SRTM-X and ASTER elevation data and its influence on topographical and hydrological modelling: case study of the Pieniny Mts. in Poland. *International Journal of Geoinformatics, 9*(2), 7–14.

Daag, A., & van Westen, C. J. (1996). Cartographic modelling of erosion in pyroclastic flow deposits of Mount Pinatubo, Philippines. *ITC Journal, 2*, 110–124.

Darmawan, H. (2012). Pyroclastic flow modeling using TITAN2D to predict the hazard of hot cloud after the 2010 eruption Merapi volcano. M.Sc. Thesis, Faculty of Geography, Gadjah Mada University. (In Indonesian).

Diefenbach, A. K., Crider, J. G., Schilling, S. P., & Dzurisin, D. (2012). Rapid, low-cost photogrammetry to monitor volcanic eruptions: an example from Mount St. Helens, Washington, USA. *Bulletin of Volcanology, 72*(2), 579–587.

d'Ozouville, N., Deffontaines, B., Benveniste, J., Wegmuller, U., Violette, S., & de Marsily, G. (2008). DEM generation using ASAR (ENVISAT) for addressing the lack of freshwater ecosystems management, Santa Cruz Island, Galapagos, Galapagos. *Remote Sensing of Environment on Monitoring Freshwater Ecosystems, 112*, 4131–4147.

Felpeto, A., Matri, J., & Ortiz, R. (2007). Automatic GIS-based system for volcanic hazard assessment. *Journal of Volcanology and Geothermal Research, 166*, 106–116.

Giribabu, D., Kumar, P., Mathew, J., Sharma, K. P., & Murthy, Y. V. N. K. (2013). DEM generation using Cartosat-1 stereo data:

issues and complexities in Himalayan terrain. *European Journal of Remote Sensing, 46*, 431–443.

GonzáLez, P.J., Singh, K.D., & Tiampo, K.F. (2014). Shallow hydrothermal pressurization before the 2010 Eruption of Mount Sinabung Volcano, Indonesia, Observed by use of ALOS Satellite Radar Interferometry. *Pure and Applied Geophysics* doi:10.1007/s00024-014-0915-7.

Hashimoto, M. (2013). Ground deformation related to active faults detected by persistent scatterer InSAR. Synthetic Aperture Radar (APSAR), Asia-Pacific Conference, pp. 477–480.

Hayakawa, Y. S., Uguchi, T., & Zhou, L. (2008). Comparison of new and existing global digital elevation models: ASTER G-DEM and SRTM-3. *Geophysical Research Letters, 35*(17), 1–5. doi:10.1029/2008GL035036.

Hirano, A., Welch, R., & Lang, H. (2003). Mapping from ASTER stereo image data: DEM validation and accuracy assessment. *ISPRS Journal of Photogrammetry and Remote Sensing, 57*(5–6), 356–370.

Huggel, C., Schneider, D., Miranda, P. J., Granados, H. D., & Kääb, A. (2008). Evaluation of ASTER and SRTM DEM data for lahar modeling: a case study on lahars from Popocatépetl Volcano, Mexico. *Journal of Volcanology and Geothermal Research, 170*, 99–110.

Indonesian Central Agency of Statistic (BPS) (2013). Government of North Sumatra. http://sumut.bps.go.id/ Cited June 08, 2015 (In Indonesian).

Surono, Jousset, P., Pallister, J., Boichu, M., Buongiorno, M.F., Budisantoso, A., et al. (2012). The 2010 explosive eruption of Java's Merapi volcano—A '100-year' event. *Journal of Volcanology and Geothermal Research 241–242*, 121–135.

Kornus, W., Alamús, R., Ruiz, A., & Talaya, J. (2006). DEM generation from SPOT-5 3-fold along track stereoscopic imagery using autocalibration. *ISPRS Journal of Photogrammetry & Remote Sensing, 60*, 147–159.

Kriswati, E., Agustan, Pamitro, Y., Hendrasto, & Trisakti, B. (2012). Volcano deformation analysis using ALOS PALSAR. In: Working Group 3, *Report and Proceedings of ALOS Application and Verification Project in Indonesia 2nd edn.*

Marfai, M. A., & King, L. (2007). Monitoring land subsidence in Semarang, Indonesia. *Environmental Geology, 53*, 651–659. doi:10.1007/s00254-007-0680-3.

Mukherjee, S., Joshi, P. K., Ghosh, A., Garg, R. D., & Mukhopadhyay, A. (2013). Evaluation of vertical accuracy of open source digital elevation model (DEM). *International Journal of Applied Earth Observation and Geoinformation, 21*, 205–217.

Murray, J. B. (1990). High-level magma transport at Mount Etna volcano, as deduced from ground deformation measurements. In M. P. Ryan (Ed.), *magma transport and storage* (pp. 357–383). London: Wiley.

Pallister, J. S., Hoblitt, R. P., Crandell, D. R., & Mullineaux, D. R. (1992). Mount St. Helens a decade after the 1980 eruptions magmatic models, chemical cycles, and a revised hazard assessment. *Bulletin of Volcanology, 54*, 126–146.

Pallister, J. S., Schneider, D. J., Griswold, J. P., Keeler, R. H., Burton, W. C., Noyles, C., et al. (2013). Merapi 2010 eruption—chronology and extrusion rates monitored with satellite radar and used in eruption forecasting. *Journal of Volcanology and Geothermal Research, 261*, 144–152.

Prush, V. B., & Lohman, R. B. (2015). Time-Varying elevation change at the Centralia coal mine in Centralia, Washington (USA). *Constrained with InSAR, ASTER, and Optical Imagery, Selected Topics in Applied Earth Observations and Remote Sensing, IEEE, 8*(2), 919–925.

Sambodo, K.A., & Soleh, M. (2011). Interferometric SAR phase unwrapping ALOS PALSAR data using least-squares algorithm two-dimensional phase unwrapping. In: Proceedings of the national geomatics SAR (GEOSARNAS), Bogor 12–13 September 2011. (In Indonesian).

Solikhin, A., Thouret, J. C., Gupta, A., Sayudi, D. S., Oehler, J. F., & Liew, S. C. (2015). Effects and behavior of pyroclastic and lahar deposits of the 2010 Merapi eruption based on high-resolution optical imagery. *3rd International Symposium on Earthquake and Disaster Mitigation. Procedia Earth and Planetary Science, 12*, 1–10.

Stevens, N. F., Wadge, G., & Murray, J. B. (1999). Lava flow volume and morphology from digitized contour maps: a case study at Mount Etna, Sicily. *Geomorphology, 28*, 251–261.

Su, J., & Bork, E. (2006). Influence of vegetation, slope, and LiDAR sampling angle on DEM accuracy. *Photogrammetric Engineering and Remote Sensing, 72*(11), 1265–1274.

Sutikno, S. (2007). Earthquake disaster of Yogyakarta and Central Java, and disaster reduction, Indonesia. *Forum Geografic, 21*(1), 1–16.

Tachikawa, T., Hato, M., Kaku, M., & Iwasaki, A. (2011). Characteristics of ASTER GDEM version 2. *Geoscience and Remote Sensing Symposium (IGARSS), IEEE,* pp. 3657–3660. doi:10.1109/IGARSS.2011.6050017.

Tadono, T., Takaku, J., Tsutsui, K., Oda, F., & Nagai, H. (2015). Status of ALOS World 3D (AW3D) global DSM generation. *Geoscience and remote sensing symposium (IGARSS), IEEE* pp. 3822–3825.

Toutin, T. H. (2010). Impact of RADARSAT-2 SAR ultrafine-mode parameters on stereo—radargrammetric DEMs. *IEEE Transactions on Geoscience and Remote Sensing, 48*(10), 3816–3823.

Trisakti, B., & Julzarika, A. (2011). DEM generation from stereo ALOS PRIMS and its quality improvement. *International Journal of Remote Sensing and Earth Sciences, 8*, 41–48.

Wang, L., Chen, J., Zhang, H, & Chen, L. (2011). Difference analysis of SRTM C-band DEM and ASTER GDEM for global land cover mapping, *In: 2011 international symposium on image and data fusion (ISIDF), Tengchong, Yunnan, 9–11 Aug. 2011, pp. 1–4, IEEE*, Piscataway, N.J.

Yulianto, F. (2014). Risk analysis of pyroclastic flows of the 2010 post-eruption of Merapi volcano using remotely sensed data and Geographic Information Systems. M.Sc. Thesis, IPB Graduate School, Bogor Agriculture University. (In Indonesian).

Yulianto, F., Sofan, P., Khomarudin, M. R., & Haidar, M. (2013). Extracting the damaging effects of the 2010 eruption of Merapi volcano in Central Java, Indonesia. *Natural Hazards, 66*, 229–247. doi:10.1007/s11069-012-0438-4.

Yulianto, F., Sofan, P., Zubaidah, A., Sukowati, K. A. D., Pasaribu, J. M., & Khomarudin, M. R. (2015a). Detecting areas affected by flood using multi-temporal ALOS PALSAR remotely sensed data in Karawang, West Java, Indonesia. *Natural Hazards, 77*, 959–985. doi:10.1007/s11069-015-1633-x.

Yulianto, F., Tjahjono, B., & Anwar, S. (2015b). The applications of Monte Carlo algorithm and energy cone model to produce the probability of block-and-ash flows of the 2010 eruption of Merapi volcano in Central Java, Indonesia. *Arabian Journal of Geosciences, 8*, 4717–4739. doi:10.1007/s12517-014-1525-5.